AIAA Journal
Vol. 47, No. 6, June 2009

Aeroacoustic Computations for Turbulent Airfoil Flows

Wen Zhong Shen,* Weijun Zhu,† and Jens Nørkær Sørensen‡
Technical University of Denmark, 2800 Lyngby, Denmark

DOI: 10.2514/1.40399

The flow-acoustic splitting technique for aeroacoustic computations is extended to simulate the propagation of acoustic waves generated by three-dimensional turbulent flows. In the flow part, a subgrid-scale turbulence model (the mixed model) is employed for large-eddy simulations. The obtained instantaneous flow solution is employed as input for the acoustic part. At low Mach numbers, the differences in scales and propagation speed between the flow and the acoustic field are quite large, and hence different meshes and time steps can be used for the two parts. The model is applied to compute flows past a NACA 0015 airfoil at a Mach number of 0.2 and a Reynolds number of 1.6×10^5 for different angles of attack. The flow solutions are validated by comparing lift and drag characteristics with experimental data. The comparisons show good agreements between the computed and measured airfoil lift characteristics for angles of attack up to stall. For the acoustic solutions, predicted noise spectra are validated quantitatively against experimental data. A parametrical study of the noise pattern for flows at angles of attack between 4 and 12 deg shows that the noise level is small for angles of attack below 8 deg, increases sharply from 8 to 10 deg, and reaches a maximum at 12 deg.

Nomenclature

C = model constant
C_d = drag coefficient
C_l = lift coefficient
c = speed of sound
D = airfoil chord
f = frequency
f^* = dimensionless frequency
k = turbulent kinetic energy
M = Mach number
$\bar{P}$ = filtered incompressible pressure
p = pressure
p_0 = ambient atmosphere pressure
p^* = acoustic pressure
Re = Reynolds number $\rho U_o D/\mu$
St = Strouhal number fD/U_o
t = time
U_i = ith incompressible velocity component
$\bar{U}_i$ = ith filtered incompressible velocity component
U_o = freestream velocity
U_i' = ith fluctuating incompressible velocity component
u_i^* = ith acoustic velocity component
x_i = ith coordinate
y^+ = dimensionless wall distance
α = model parameter
β = axis angle
γ = specific heat ratio
Δ = average grid size
Δ_i = grid size in the x_i direction
δ_{ij} = Kronecker symbol
ν = kinematic viscosity
ν_t = eddy viscosity
ρ = density
ρ_0 = ambient density
ρ^* = acoustic density
τ_{ij} = turbulent stress
ϕ = angle of attack
$\boldsymbol{\omega}$ = vorticity

Introduction

AEROACOUSTIC noise from wind turbines may be a cause of annoyance from people living in the neighborhood of the turbines. This may cause problems with respect to public acceptance of wind turbines and hamper the further development of wind power. To ensure a continuous development of wind power, it is therefore required to develop techniques for modeling and reducing wind turbine noise. The flow about wind turbines is usually complex and turbulent and the generated noise is broadband with or without, depending on the actual flow case, a dominant frequency. The simplest way of predicting noise is to employ a semi-empirical model in which the blades are divided into two-dimensional airfoil sections and to determine the total noise emission as the sum of the contribution of each element. The airfoil self-noise on each section is considered as a sum of five different mechanisms, and each mechanism is associated with a noise formula resulting from the acoustic analogy [1–4], scaled on a set of experimental data. Semi-empirical models [5–12] are fast to run on a personal computer and can be used for designing low-noise blades. Because semi-empirical models are based on a few sets of experimental data, many fundamental questions may arise, such as the applicability of the model and the accuracy of the experimental data. To obtain more detailed data, a possibility is to solve the 3-D compressible Navier–Stokes equations using large-eddy simulations (LES). Because computer power and capacity have been improved a lot (about 10 times every five years from statistics of the last 20 years), and it will be increased further, computational aeroacoustics with LES is now becoming a valuable complementary numerical tool to the semi-empirical models. For a comprehensive introduction to the area of acoustics with large-eddy simulation, the reader is referred to [13].

A first step for studying noise emission from wind turbines is to consider airfoil flows. Noise generated from airfoils has been studied intensively in the past four decades by many researchers using experimental tools or numerical simulations. Smith et al. [14], Clark [15], and Hersh and Hayden [16] showed experimentally that discrete tonal noise is emitted from airfoils. Several studies, such as by Paterson et al. [17], Sunyach et al. [18], Tam [19], Fink [20], and Arbey and Bataille [21], were dealing with the understanding of tonal noise. The tonal noise problem was intensively studied by Lowson

---

Received 13 August 2008; revision received 19 December 2008; accepted for publication 26 February 2009. Copyright © 2009 by the American Institute of Aeronautics and Astronautics, Inc. All rights reserved. Copies of this paper may be made for personal or internal use, on condition that the copier pay the $10.00 per-copy fee to the Copyright Clearance Center, Inc., 222 Rosewood Drive, Danvers, MA 01923; include the code 0001-1452/09 $10.00 in correspondence with the CCC.

[*] Associate Professor, Department of Mechanical Engineering, Center for Fluid Dynamics, Building 403; shen@mek.dtu.dk.

[†] Postdoctoral Student, Department of Mechanical Engineering, Center for Fluid Dynamics, Building 403.

[‡] Professor, Department of Mechanical Engineering, Center for Fluid Dynamics, Building 403.

et al. [22], Nash and Lowson [23], Lowson et al. [24], McAlpine et al. [25], and Nash et al. [26]. Using a three-component laser Doppler anemometry technique, they showed that the tonal noise is mainly created from the amplified Tollmien–Schlichting waves on the pressure side of the airfoil. Desquesnes et al. [27] showed similar behavior using 2-D direct numerical simulations. Sandberg and Sandham [28] and Wang and Moin [29] studied the trailing-edge noise generated by turbulent boundary layers. Recently, Marsden et al. [30] studied the noise generation from a NACA 0012 airfoil at a Mach number of 0.22 and zero angle of attack by directly solving the compressible equations with large-eddy simulation. Most of the preceding studies were dealing with tonal noise generated for flow past a NACA 0012 airfoil at small angles of attack and small Mach numbers.

At low Mach numbers M, the length scale of the flow is about M times smaller than the acoustic wavelength, and the propagating speed of acoustic waves is $1/M$ time faster than the flow convection speed. For such low Mach number flows, it is rather computationally expensive to consider flow and acoustics together by solving the compressible Navier–Stokes equations. To consider them separately, the splitting technique developed by Shen and Sørensen [31] is used. In this method, the solution is divided into two steps. In the first step, a flow solution is obtained by solving the incompressible Navier–Stokes equations together with a suitable subgrid-scale (SGS) model. In our simulations, the mixed turbulence model developed by Ta Phuoc [32] and Tenaud et al. [33] is used. The mixed model exploits the advantage of combining a closure based on vorticity with the small-scale similarity turbulence model of Bardina et al. [34], and it constitutes a simple and efficient alternative to the dynamic SGS model. After the initial transients of the flow are damped out, the solution of the acoustic perturbation equations is initiated. Because the flow equations and the acoustic equations are solved separately in two steps, they can be discretized on two different meshes with two different time steps. For this reason, the splitting technique is several times faster than methods based on solving directly the compressible Navier–Stokes equations.

The paper is organized as follows. The numerical methods for both flow and acoustics are summarized in the next section, and numerical results of three-dimensional flows past a NACA 0015 airfoil are presented and discussed in the following section.

Numerical Method

For flows at low Mach numbers, the scales and the propagation speeds of the flow and the acoustic waves are quite different. Therefore, it is advantageous to consider them separately. The viscous-acoustic splitting technique developed for turbulent flows in [31] uses a decomposition of the compressible Navier–Stokes equations into an incompressible part that governs flow motions and a perturbed compressible part that is responsible for the acoustics. In this section, the governing equations for both flow and acoustics are presented and followed by a brief description of their numerical discretizations.

Flow Equations

The governing equations for the flow are the three-dimensional incompressible Navier–Stokes equations. Because turbulent flows are considered, small-scale turbulence has to be modeled. For this purpose, we employ LES, in which the large scales are simulated and the small scales are modeled by an eddy-viscosity-based subgrid-scale model. Two spatial filters are used in the simulations. The first filter, identified by a bar ($\bar{\ }$), is due to the finest mesh used in the computations, and the second filter, denoted as the test filter, is shown with a tilde ($\tilde{\ }$). The second filter is chosen to be twice coarser than the finest mesh. The filtered incompressible Navier–Stokes equations in velocity-pressure variables are written

$$\frac{\partial \bar{U}_i}{\partial t} + \frac{\partial(\bar{U}_i \bar{U}_j)}{\partial x_j} = -\frac{1}{\rho}\frac{\partial \bar{P}}{\partial x_i} + \nu \frac{\partial^2 \bar{U}_i}{\partial x_j^2} + \frac{\partial \tau_{ij}}{\partial x_j} \tag{1}$$

$$\frac{\partial \bar{U}_i}{\partial x_i} = 0 \tag{2}$$

In Eq. (1), the turbulent stresses from the filtering are expressed as

$$\tau_{ij} = \bar{U}_i \bar{U}_j - \overline{U_i U_j} = (\bar{U}_i \bar{U}_j - \overline{\bar{U}_i \bar{U}_j}) - (\overline{\bar{U}_i U'_j + U'_i \bar{U}_j}) - \overline{U'_i U'_j} \tag{3}$$

where the fluctuations are defined as $U'_i = U_i - \bar{U}_i$. The turbulent stresses are modeled with an eddy viscosity:

$$\tau_{ij} = \nu_t \left(\frac{\partial \bar{U}_i}{\partial x_j} + \frac{\partial \bar{U}_j}{\partial x_i} \right) - \frac{2}{3} k \delta_{ij} \tag{4}$$

The eddy viscosity is determined by the mixed-scale turbulence model introduced by Ta Phuoc [32]:

$$\nu_t = C |\bar{\omega}|^{\alpha} k^{(1-\alpha)/2} \Delta^{(1+\alpha)} \tag{5}$$

where $\Delta = (\Delta_x \Delta_y \Delta_z)^{1/3}$ is an average grid size, and α is a parameter that takes a value between 0 and 1. Assuming similarity between two grid levels, the turbulent kinetic energy can be estimated by using the second filter:

$$k = \frac{1}{2} \sum_{j=1}^{3} (U_j - \bar{U}_j)^2 \approx \frac{1}{2} \sum_{j=1}^{3} (\bar{U}_j - \tilde{\bar{U}}_j)^2 \tag{6}$$

where $\tilde{\bar{U}}_j$ is the double-filtered velocity obtained by applying the second filter on the resolved velocity $\bar{U}_j$. The model Eq. (5) becomes a pure vorticity-based model in the case when $\alpha = 1$,

$$\nu_t = C |\bar{\omega}| \Delta^2 \tag{7}$$

and it becomes the Bardina model [34] in the case when $\alpha = 0$:

$$\nu_t = C k^{1/2} \Delta \tag{8}$$

From studies on the model parameter in [32,35], it was found that the model generally performs best when the parameter is chosen to be $\alpha = 0.5$,

$$\nu_t = C |\bar{\omega}|^{1/2} k^{1/4} \Delta^{3/2} \tag{9}$$

with $C = 0.02$.

The filtered incompressible equations are solved by the EllipSys3D code, which was developed at the Technical University of Denmark [36] in cooperation with the Department of Wind Energy at Risø National Laboratory [37]. The EllipSys3D code is based on a multiblock/cell-centered finite volume discretization of the steady/unsteady incompressible Navier–Stokes equations in primitive variables (pressure velocity). The predictor–corrector method is used. In the predictor step, the momentum equations are discretized using a second-order backward-differentiation scheme in time and second-order central differences in space, except for the convective terms that are discretized by the QUICK upwind scheme. In the corrector step, the improved Rhie–Chow interpolation developed by Shen et al. [38] is used to avoid numerical oscillations from pressure decoupling. Because there are no optimal values for the relaxation parameters in the unsteady SIMPLE algorithm, the solution is slightly dependent on the choice of the parameters. To make it more consistent, the improved SIMPLEC scheme on collocated grids [39] is used, which makes the solution independent of the relaxation parameters. The obtained Poisson pressure equation is solved by a five-level multigrid technique. For more details about the numerical technique, the reader is referred to [36–39]. Because the EllipSys3D code is programmed using a multiblock topology, it can relatively easily be parallelized using a message-passing interface.

Acoustic Equations

The three-dimensional acoustic/compressible perturbation equations for turbulent flows, developed in [31], were obtained by subtracting the viscous incompressible solution from the compressible Navier–Stokes equations and neglecting the turbulent quantities contained in the acoustic variables. The reasons for neglecting these are as follows:

1) The turbulent terms are unknown and require an additional closure.

2) The energy contained in the acoustic waves are negligible as compared with the energy of the flow quantities.

3) Acoustic sound at low Mach numbers is generated purely by the fluctuations of hydrodynamic flow quantities.

The final set of equations consists of one density equation, three velocity fluctuation equations, and one pressure correlation equation:

$$\frac{\partial \rho^*}{\partial t} + \frac{\partial f_i}{\partial x_i} = 0 \tag{10}$$

$$\frac{\partial f_i}{\partial t} + \frac{\partial}{\partial x_j}\left[f_i(\bar{U}_j + u_j^*) + \rho_0 \bar{U}_i u_j^* + \left(p^* + \frac{2}{3}\rho^* k\right)\delta_{ij}\right] = \frac{\partial}{\partial x_j}\left[\rho^* \nu_t \left(\frac{\partial \bar{U}_i}{\partial x_j} + \frac{\partial \bar{U}_j}{\partial x_i}\right)\right] \tag{11}$$

$$\frac{\partial p^*}{\partial t} - c^2 \frac{\partial \rho^*}{\partial t} = -\frac{\partial \bar{P}}{\partial t} \tag{12}$$

where the asterisk (*) denotes acoustic variables, with auxiliary variables defined as $f_i = \rho u_i^* + \rho^* \bar{U}_i$. The speed of sound is calculated from the following expression, valid for real gases:

$$c^2 = \frac{\gamma(\bar{P} + p^*)}{\rho_0 + \rho^*} \tag{13}$$

The acoustic perturbation equations are discretized using the decretization method developed in [40]. As for the flow equations, the predictor–corrector/finite volume method is also used for solving the acoustic equations. In the predictor step, the momentum equations are discretized using a second-order Crank–Nicolson scheme in time, which is much less dissipative than the backward-differentiation scheme used for the flow equations and second-order central differences in space, except for the convective terms that are discretized by the QUICK upwind scheme. In the corrector step, the modified SIMPLEC scheme on collocated grids is used together with the improved Rhie–Chow interpolation technique. The obtained pressure-correction equation is solved by using the same multigrid technique that is used in the flow part.

Meshes

As two-dimensional flows past airfoils are unstable to three-dimensional perturbations at moderate or high Reynolds numbers (bigger than about 500), it is required to model and simulate three-dimensional flows. To reduce the computational costs, periodic boundary conditions are employed in the spanwise direction. The computational domain used for the flow computations covers a cylindrical domain with a radius of about 40 airfoil chords and of 2 airfoil chords in the spanwise direction. The mesh consists of 192 cells highly stretched from the wall in the radial direction, 256 cells in the azimuth direction, and 64 cells uniformly distributed in the spanwise direction. To estimate the resolution near the wall, the y^+ values at the first points away from the airfoil surface are calculated at a Reynolds number of 1.6×10^5 and an angle of attack of 12 deg. Using the shear stress expression in the viscous sublayer, the y^+ values were found to be about 6 on the pressure side and about 2.5 on the suction side. The y^+ value on the pressure side is slightly bigger than the limit y^+ value in the viscous sublayer. A discussion on near wall resolution is presented in the next section. The computations were performed on 12 processors.

The same number of mesh points is used in the acoustic computations. Because acoustic waves are generated from the airfoil and propagate outward in all directions, a relatively finer mesh is required in the far field. On the other hand, fewer points are needed close to the wall, because the acoustic sources are contained in the incompressible solution. To not increase the communication time between blocks, the mesh redistribution is carried out within the same block. Near the walls, a coarser mesh is created, with the first grid cells near the walls being 2 times larger than those of the flow mesh. A relative finer mesh is generated in the far field. In the spanwise direction, the original mesh size is kept. Note that it is difficult to generate a coarser mesh near the walls within the same block. Thus, based on the flow mesh, a mesh for the acoustic computations is generated in a small cylindrical domain with a radius of about 22 chords and of 2 chords in the spanwise direction.

Because acoustic waves propagate at sound speed, a much smaller acoustic time step than the flow time step is required for low Mach number flows. A coarser acoustic mesh near the walls means that a larger acoustic time step can be used. In our acoustic computations, 4–5 acoustic time steps are used at each flow time step (a dimensionless time step of 10^{-3} based on freestream velocity and airfoil chord). To get an idea about the resolution on the acoustic mesh, the number of grid points for a given frequency is estimated. For the case of an airfoil with a chord of 10 cm in a freestream velocity of 71.3 m/s, one wavelength of a frequency of about 3.8 kHz contains about 4 cells at an observer located 12 chord lengths away from the airfoil center. This shows that the spectrum up to about 4 kHz can be captured by the mesh and higher frequencies requires further refinements of the mesh.

The incompressible velocity and pressure are interpolated from the incompressible mesh to the acoustic mesh using linear interpolations. To discretize the acoustic momentum equations (11) with a finite volume approach, the source terms are first calculated on the incompressible mesh with the acoustic density interpolated from the acoustic mesh to the incompressible mesh. Next, integration of the source terms is performed on the acoustic mesh.

Results and Discussion

The main objective of our work is to develop a code capable of determining noise from wind turbines. For wind turbines, the thickness of the cross section near the blade tip is approximately 15% and the dominant noise source is located on this part. To investigate such airfoils, three-dimensional computations of turbulent flows past a NACA 0015 airfoil at a Reynolds number of 1.6×10^5 are performed. To reduce the computational time, the flow part of the code is first run. When the flow stabilizes at a dimensionless time of about 80, based on freestream velocity and airfoil chord, the acoustic part of the code starts to run together with the flow part. To get an acoustic signal suitable for Fourier analysis, we perform 80,000 flow iterations, corresponding to a dimensionless time of 80. All computations were carried out on a PC cluster consisting of 210 2.4 GHz processors. Each turbulent flow case requires a computational time corresponding to about 2 months of nonstop computations on 12 processors.

Table 1 Mean lift and drag coefficients calculated on a domain with different sizes in the spanwise direction (x_3) for flow past a NACA 0015 airfoil at a Reynolds number of 1.6×10^5, and an angle of attack of 12 deg

x_3	1	2	3	5	6
Cl	1.0629	0.6248	0.6280	0.6132	0.6120
Cd	0.0773	0.1668	0.1648	0.1560	0.1542

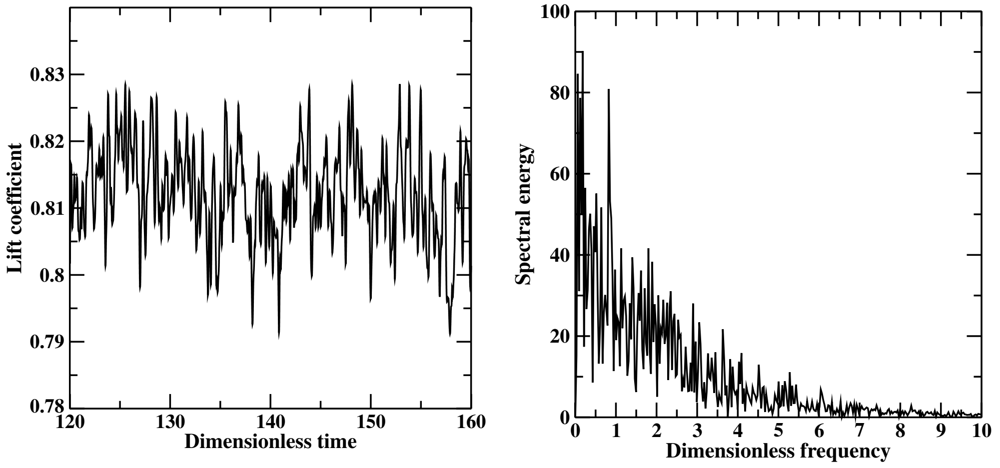

a) b)

Fig. 1 Plots of a) lift coefficient and b) frequency spectrum of the lift coefficient for flow past a NACA 0015 airfoil at a Reynolds number of 1.6×10^5 and an angle of attack of 8 deg.

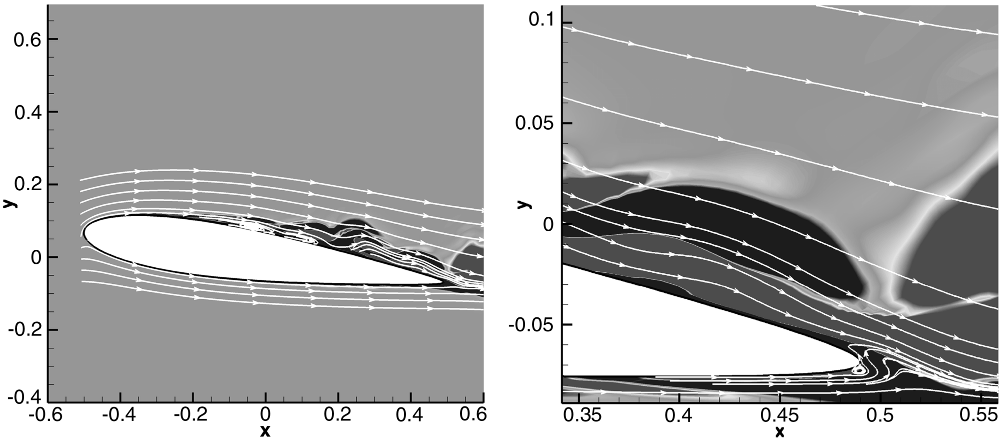

a) b)

Fig. 2 Plots of a) streamwise vorticity and streamlines on a cross section and b) zoomed region near the trailing edge for flow past a NACA 0015 airfoil at a Reynolds number of 1.6×10^5 and an angle of attack of 8 deg.

Flow Solutions

For large-eddy simulations, it is known that a very fine mesh is required for flows at high Reynolds numbers. As a compromise between computer capacity and accuracy, turbulent flows past a NACA 0015 airfoil at a Reynolds number of 1.6×10^5 are computed with periodic boundary conditions in the spanwise direction. Before making the final computations, two computations for testing the employed numerical code are performed. The first test is to identify the significance of numerical dissipation when using a second-order-accurate finite volume code. This task addresses the question of whether a second-order (low-order) code can be used for large-eddy simulations. Computations both with and without a SGS model are carried out for the flow past a NACA 0015 airfoil at a Reynolds number of 1.6×10^5, an angle of attack of 12 deg, and a spanwise width of 2 chords.

The obtained results show that the solution calculated without a SGS model is almost two-dimensional (not relevant), whereas the solution with the SGS model is fully three-dimensional. As a consequence, the mean lift coefficient predicted by the solver without a SGS model is bigger than in the case with the SGS model. On the other hand, the mean drag coefficient without a SGS model is slightly smaller than with a SGS model, due to the missing eddy viscosity in the former case. This demonstrates that the SGS model is active and that the solution is not dominated by artificial numerical dissipations. The second test is to find a suitable size of the spanwise domain. At a high angle of attack, the wake structure of the Kármán vortex street is rather big. To verify if a spanwise width of 2 chords is enough, computations with spanwise distances of 1, 2, 3, 5, and 6 chords, respectively, with the same number of mesh points are performed. The obtained mean lift and drag coefficients are shown in Table 1. The lift and drag coefficients are almost the same within acceptable accuracy for the spanwise size larger than 2 chords, whereas the

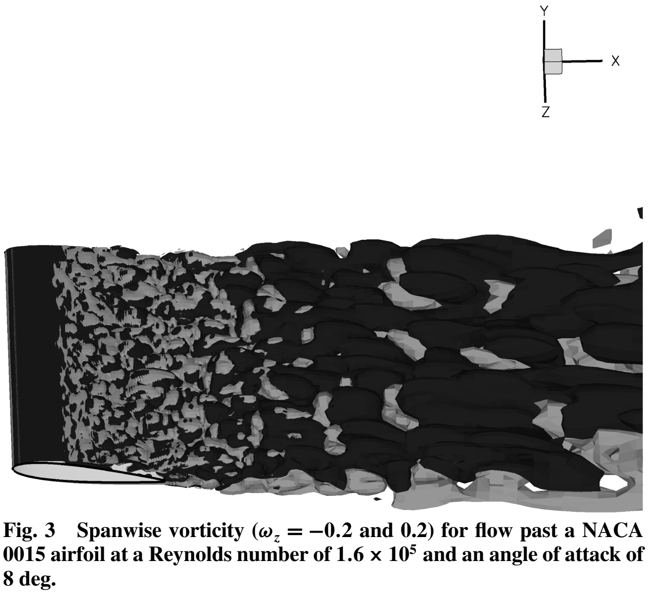

Fig. 3 Spanwise vorticity ($\omega_z = -0.2$ and 0.2) for flow past a NACA 0015 airfoil at a Reynolds number of 1.6×10^5 and an angle of attack of 8 deg.

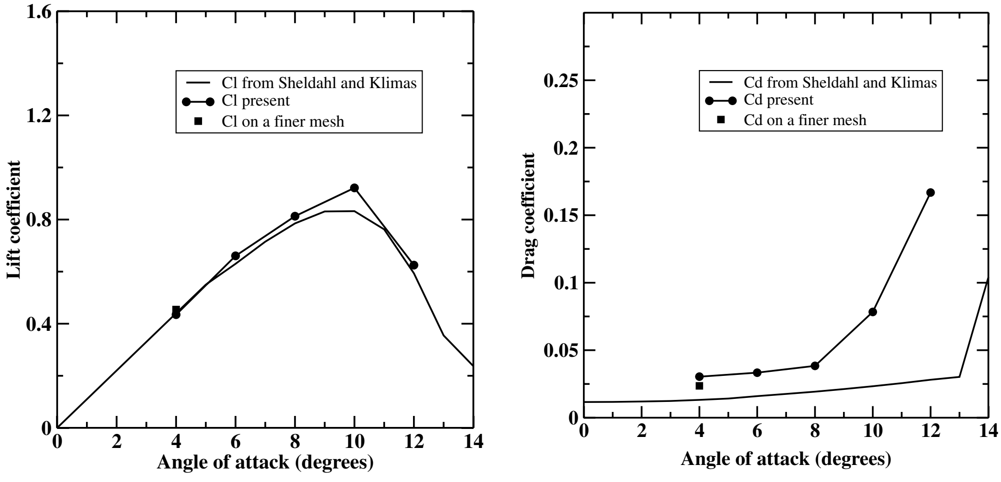

a) b)

Fig. 4 Comparisons between computations and experiments (Sheldahl and Klimas [41]) of a) lift coefficient and b) drag coefficient for flow past a NACA 0015 airfoil at a Reynolds number of 1.6 × 10^5.

computation with a spanwise size of 1 chord gives different results. The lift and drag fluctuations are in the same order for the cases with a spanwise size larger than 2 chords. Hence, we can conclude that a spanwise distance of 2 chords is sufficient to cover the low-frequency structure in the spanwise direction.

Next, turbulent flow past a NACA 0015 airfoil at a Reynolds number of 1.6×10^5 and an angle of attack of 8 deg with periodic boundary conditions in the spanwise direction is computed. The computed lift coefficient, shown in Fig. 1a, contains many small fluctuations around a mean C_l value of 0.813. The time signal of the lift coefficient is analyzed by applying a fast Fourier transform (FFT) on a time series consisting of $32,768 = 2^{15}$ data points. The frequency spectrum is shown in Fig. 1b. The dominant dimensionless frequency (the Strouhal number) attains a value of about 0.82. The inner part of the spectrum is dominated by some strong peaks, indicating the existence of low-frequency modes. Because of the time length of the signal (about $T = 32$), frequencies less than about 0.03 cannot be captured. However, a dominant frequency of about 0.18 shows the existence of low-frequency modes. The low frequencies correspond to the structural phase change in the spanwise direction. The spanwise vorticity and streamlines are plotted in Fig. 2, in which the vortices are seen to be produced on the suction side of the airfoil section. A closer view at the flow structures in Fig. 2b reveals that a vortex shedding occurs at the trailing edge. The streamwise vorticity is clearly three-dimensional, as shown in Fig. 3. It is also seen that the flow starts to separate at a point around 0.3 chords from the leading edge on the suction side. Note that the separation point is rather unstable and does not remain at the same chordwise position during the computations. Eddies close to the airfoil surface are quite small and only big eddies are seen downstream of the trailing edge, because the smallest eddies are smoothed out by the relative coarse mesh in the wake.

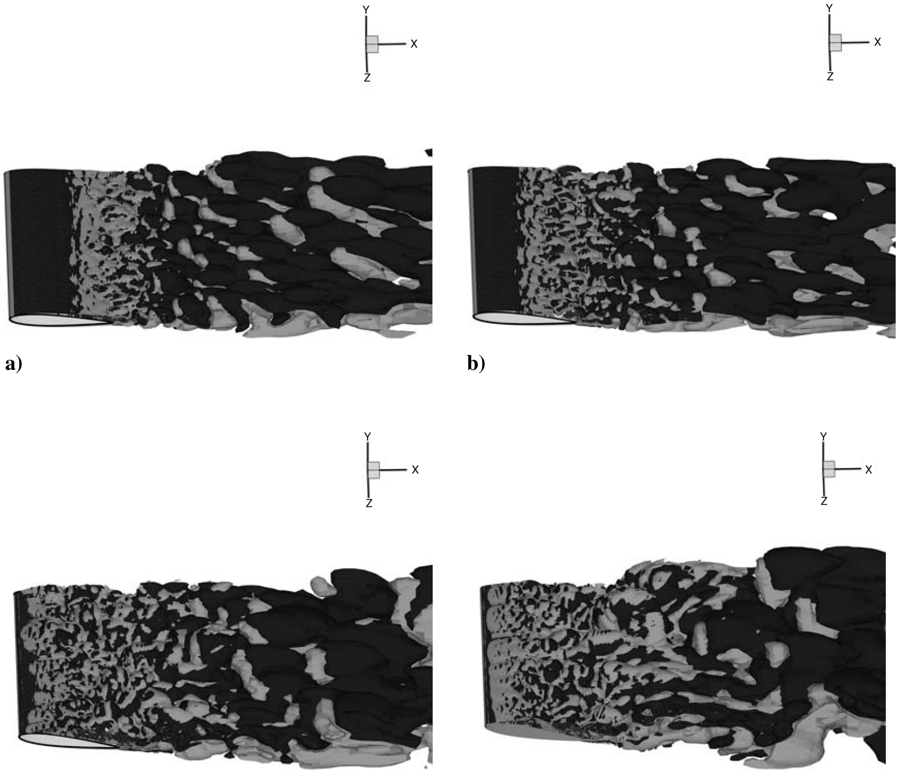

c) d)

Fig. 5 Spanwise vorticity plots for flows past a NACA 0015 airfoil at a Reynolds number of 1.6 × 10^5 and angles of attack of a) 4 deg, b) 6 deg, c) 10 deg, and d) 12 deg.

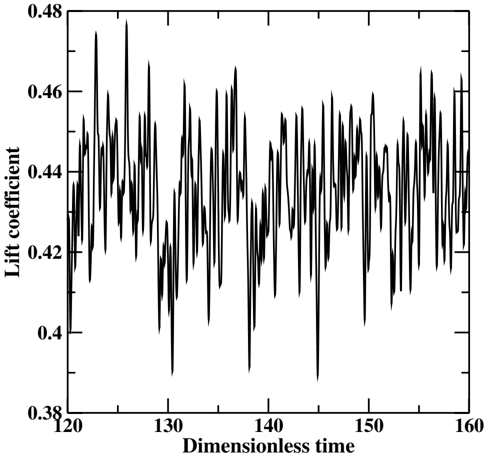

Fig. 6 Lift coefficient for flow past a NACA 0015 airfoil at a Reynolds number of 1.6 × 10^5 and an angle of attack of 4 deg.

To further validate the flow solver, flows past a NACA 0015 airfoil are computed at different angles of attack and the outcome is compared with the experimental data by Sheldahl and Klimas [41]. Lift and drag coefficients are plotted in Fig. 4. From the figure, good agreements between the measured and computed lift coefficients are seen for angles of attack below 8 deg. At higher angles of attack (10 and 12 deg), the computed maximum lift coefficient is slightly overpredicted as compared with the experimental data [41]. The drag coefficient is plotted in Fig. 4b. The computed drag coefficient is about twice as big as the measured value for incidences up to about 8 deg. For higher incidences when the airfoil undergoes stall, the discrepancy becomes even more serious. Because the computations already are very time-demanding, it was not possible to increase the number of mesh points to further check the influence of the total number of mesh points. Instead, the mesh was redistributed such that twice as many points were concentrated near the surface of the airfoil. However, this had only a minor impact on the results, as can be seen from the additional data points in Fig. 4. On the other hand, because the drag in all cases is small compared with the lift and because the lift coefficient for all incidences except 10 deg is in good agreement with measured data, we expect that the most significant noise sources are captured by the flow solutions.

To examine the change in the flow structures when the angle of attack increases, the spanwise vorticity is plotted in Figs. 5a–5d at angles of attack of 4, 6, 10, and 12 deg, respectively. It is displayed in the figure that the separation line moves from a position of about midchord at 4 deg to the very leading edge at 12 deg when increasing the angle of attack. The vorticity contours consist of structures or eddies of varying size, indicating the genesis of the broadband noise sources. At increasing angles of attack, eddies move closer to the leading edge and the number of small-scale eddies increases. However, it seems that the size of the largest structures, having a length scale of about a chord length, is invariant to angle-of-attack changes, whereas the smallest scales become even smaller. Looking

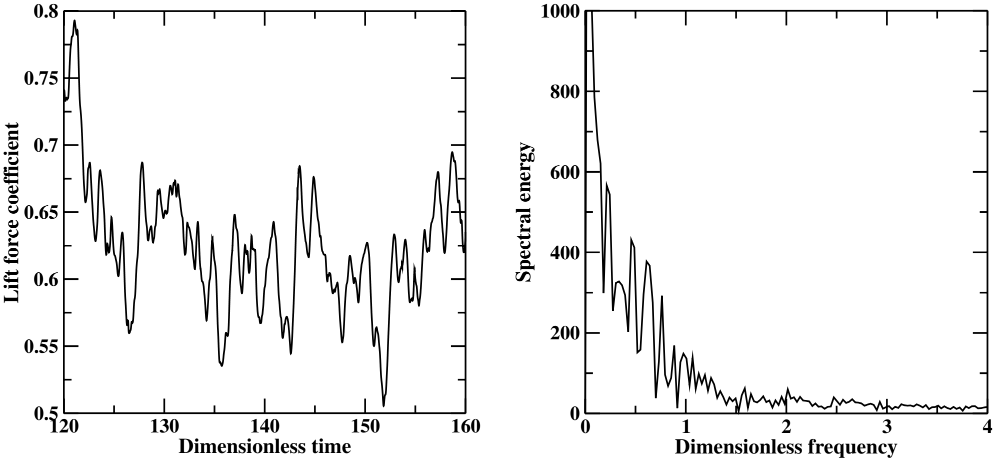

a) b)

Fig. 7 Plots of a) lift coefficient and b) frequency spectrum of the lift coefficient for flow past a NACA 0015 airfoil at a Reynolds number of 1.6 × 10^5 and an angle of attack of 12 deg.

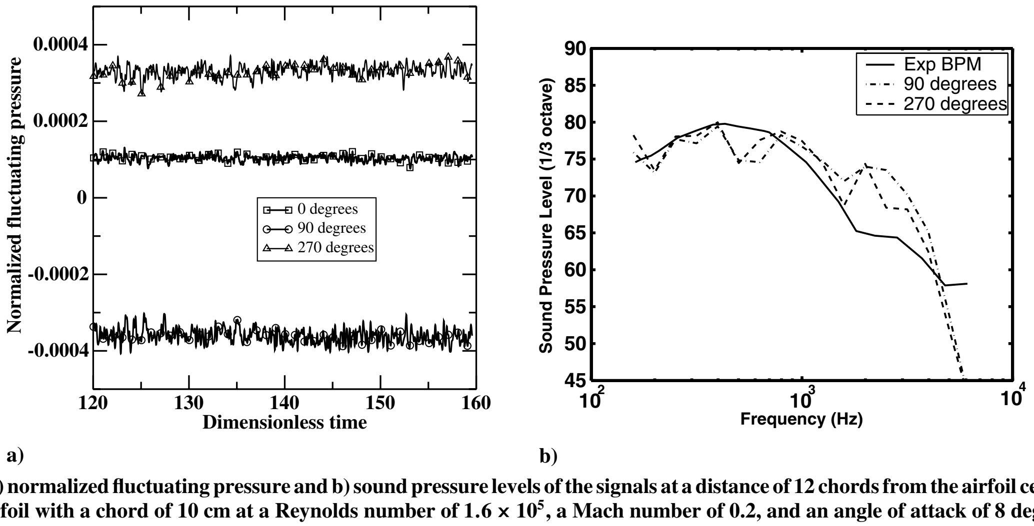

a) b)

Fig. 8 Plots of a) normalized fluctuating pressure and b) sound pressure levels of the signals at a distance of 12 chords from the airfoil center for flow past a NACA 0015 airfoil with a chord of 10 cm at a Reynolds number of 1.6 × 10^5, a Mach number of 0.2, and an angle of attack of 8 deg.

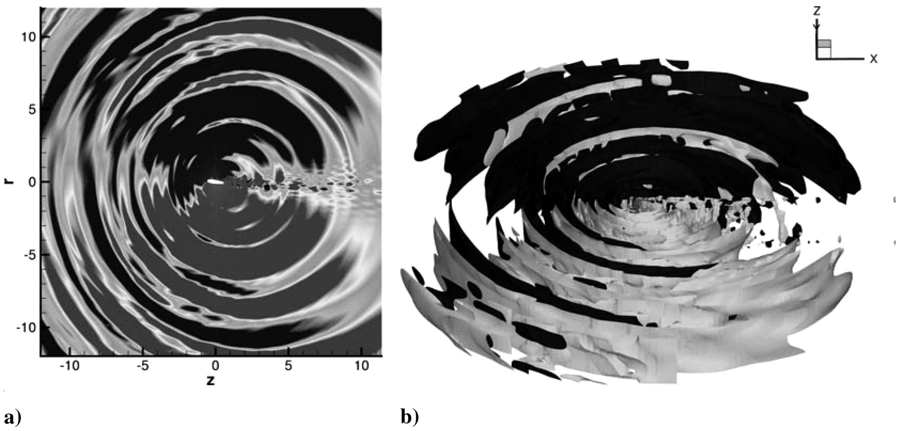

Fig. 9 Plots of a) cross-sectional and b) 3-D fluctuating pressure for flow past a NACA 0015 airfoil at a Reynolds number of 1.6 × 10^5, a Mach number of 0.2, and an angle of attack of 8 deg.

more closely at the vorticity plots, it is seen that the wake at an angle of attack of 4 deg is subject to stronger fluctuations than at 6 or 8 deg. To investigate this phenomenon, the temporal behavior of lift force coefficient at 4 deg is plotted in Fig. 6. From the figure, it is seen that the fluctuations at 4 deg are almost 3 times bigger than the fluctuations at 8 deg (see also Fig. 1a). These fluctuations about the lift force originate from the convection of big vortices along the airfoil surface and the vortex shedding at the trailing edge. The lift force coefficient at an angle of attack of 12 deg is in Fig. 7a plotted as function of time. From the figure, it is seen that low frequencies are quite pronounced. The corresponding frequency spectrum is plotted in Fig. 7b. The figure shows that the spectrum contains dominant tonal frequencies in the low-frequency region (below 1).

Acoustic Solutions

Figure 8a shows normalized fluctuating pressures $(p - p_o)/p_o$ measured at a distance of 12 airfoil chords from the airfoil center and azimuth angles of 0 deg (upstream), 90 deg (suction side), and 270 deg (pressure side), respectively, for flow past a NACA 0015 airfoil at $Re = 1.6 \times 10^5$, $M = 0.2$, and $\alpha = 8$ deg. As presented in the figure, the signals are fluctuating randomly. As reference pressure we employ the ambient pressure far upstream from the airfoil; thus, the fluctuating pressure attains positive values at 270 deg (pressure side) and negative values at 90 deg (suction side). By performing FFTs on about 32 time units signals at 90 and 270 deg using 2^{15} data points, one-third-octave spectra are obtained and plotted in Fig. 8b. To check if the model captures the experimental noise patterns, the results are compared with measured values. Unfortunately, there exist very few high-quality experimental data at low Reynolds numbers that include both flow and acoustic quantities. As a compromise, the experimental noise spectra from Brook et al. [5] are used for comparisons. The experimental noise spectrum used here was obtained for flow past a NACA 0012 airfoil with a sharp trailing edge at a Reynolds number of 5×10^5 and an angle of attack of 8.9 deg, with the observer point located at 90 deg and 1.2 m away from the airfoil. The experimental data were obtained for an airfoil with a chord of $D = 10$ cm in a flow with a freestream velocity of 71.3 m/s (experimental conditions). The computed spectra of sound pressure level (SPL) are rescaled as follows:

$$\begin{cases} f = \frac{f^* \cdot U_0}{D} \\ \mathrm{SPL} = 20\log_{10}(\frac{S\rho U_o^2}{\sqrt{2N}P_{\mathrm{ref}}}) \end{cases}$$

where S and N are the spectral energy and the number of data points from the FFT, respectively, and P_{ref} is commonly taken to be 2×10^{-5} Pa. Note that the Reynolds number and the angle of attack are kept unchanged. From the figure, it is seen that the noise is broadband and that the numerical spectra display similar sound pressure levels as in the experiment. In the low-frequency region (less than 1000 Hz), the numerical noise level is slightly smaller than the measured level, whereas in the high-frequency region (greater than 1000 Hz), it is bigger than the noise level in the experiment. This

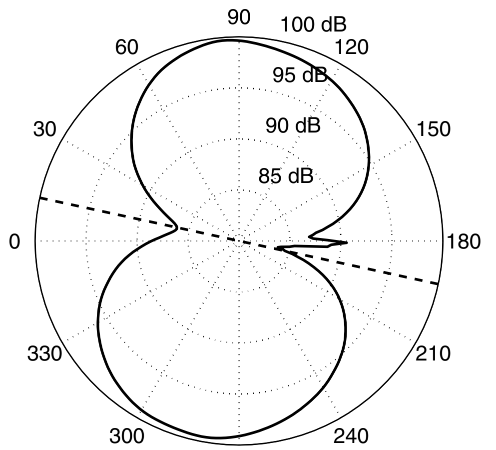

Fig. 10 Directivity pattern at a distance of 12 chords from the airfoil center for flow past a NACA 0015 airfoil at a Reynolds number of 1.6 × 10^5, a Mach number of 0.2, and an angle of attack of 8 deg.

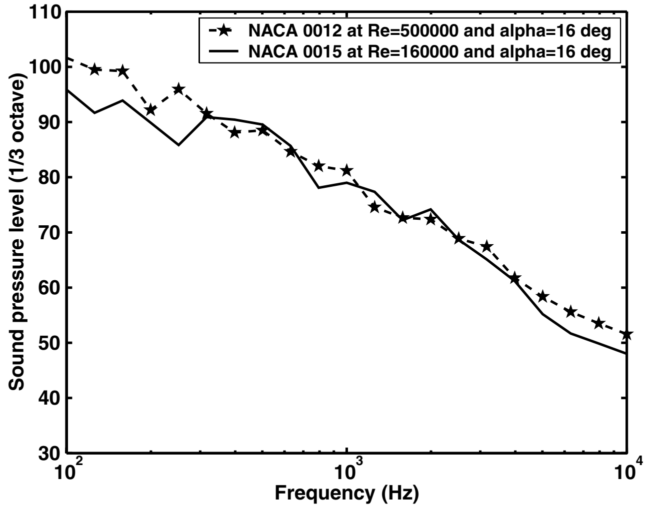

Fig. 11 Sound pressure levels of the signals measured at a distance of 12 chords from the airfoil center for flow past a NACA 0015 airfoil with a chord of 10 cm at a Reynolds number of 1.6 × 10^5, a Mach number of 0.2, and an angle of attack of 16 deg and for flow past a NACA 0012 airfoil with a chord of 10 cm at a Reynolds number of 5 × 10^5, a Mach number of 0.2, and an angle of attack of 16 deg.

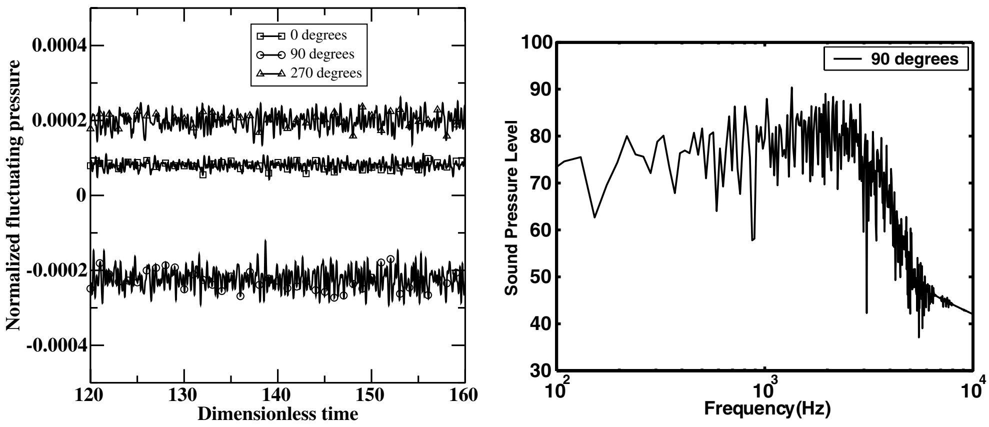

a) b)

Fig. 12 Plots of a) normalized fluctuating pressure and b) sound pressure levels of the signal at a distance of 12 chords from the airfoil center for flow past a NACA 0015 airfoil with a chord of 10 cm at a Reynolds number of 1.6 × 10^5, a Mach number of 0.2, and an angle of attack of 4 deg.

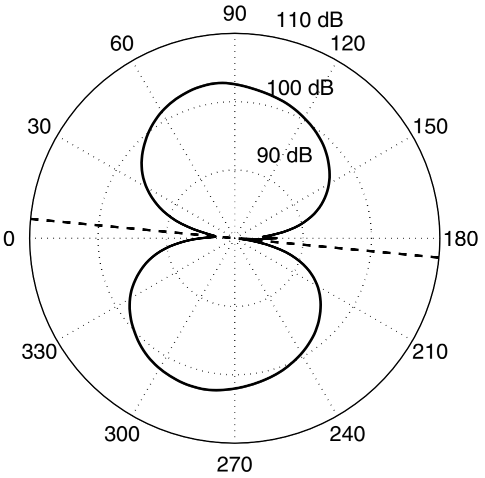

Fig. 13 Directivity pattern at a distance of 12 chords from the airfoil center for flow past a NACA 0015 airfoil with a chord of 10 cm at a Reynolds number of 1.6 × 10^5, a Mach number of 0.2, and an angle of attack of 4 deg.

is due to the difference in airfoil bluntness. The NACA 0015 airfoil used in our computations has a bluntness of about 0.013 chords, corresponding to a bluntness of 1.3 mm for the considered airfoil. As the trailing-edge bluntness is usually much smaller than the airfoil chord, the bluntness noise appears always in the high-frequency range.

Figure 9a displays a sectional plot of the fluctuating pressure. The acoustic waves are seen to mainly propagate outward from the airfoil, with the wave origin at the trailing edge. The structure of the acoustic wave is very like a dipole. Note that the mean values below the airfoil are positive, whereas the mean values above the airfoil are negative, as observed in Fig. 8a. The 3-D isosurface plot of the fluctuating pressure is shown in Fig. 9b. The plot shows that the spanwise variations are important. One may also remark that the far field is less noisy in the regions in front of and behind the airfoil. The acoustic directivity pattern for the turbulent flow is presented in Fig. 10 at a radial distance of 12 chords. From the figure, a near dipole structure is found. Dipole noise is often called unsteady loading noise and is usually created from the interaction between the (laminar or turbulent) boundary layer on the airfoil surface and the trailing edge. The axis of the near dipole has an angle of about 12.2 deg from the horizontal axis. The noise level reaches its maximum value at an azimuth angle of about 85.5 deg. In the wake region (around 180 deg), the spectrum shows a lobe structure that is created by the vorticity convection in the airfoil wake.

Because we use the experimental data at a different thickness, the dependency on airfoil thickness needs to be investigated. Zhou and Joseph [42] considered the dependency of a flat plate, a NACA 0012 airfoil, and a NACA 0024 airfoil using a frequency-domain numerical method in which the unsteady loading is obtained from thin airfoil theory. They found that the difference in sound pressure

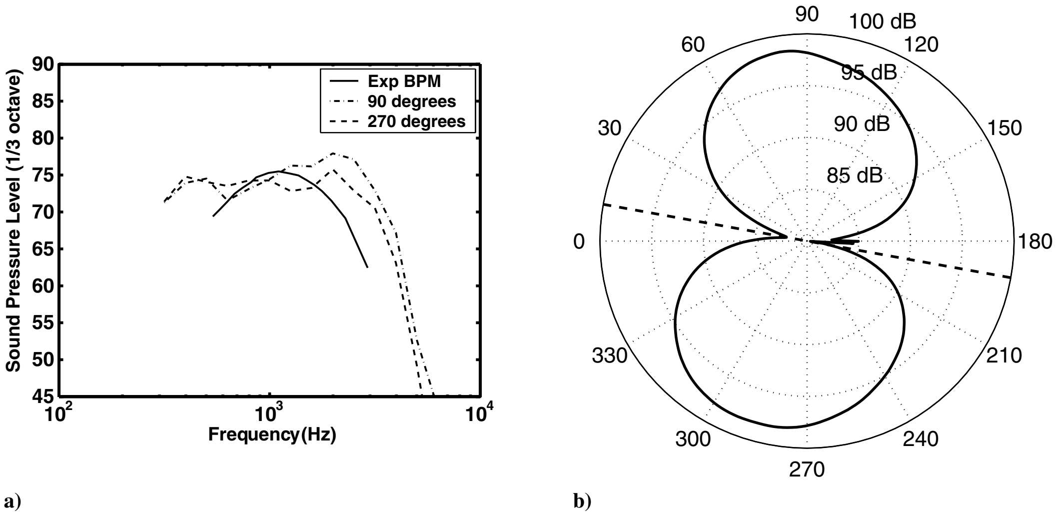

a) b)

Fig. 14 Plots of a) sound pressure levels and b) directivity pattern at a distance of 12 chords from the airfoil center for flow past a NACA 0015 airfoil with a chord of 10 cm at a Reynolds number of 1.6 × 10^5, a Mach number of 0.2, and an angle of attack of 6 deg.

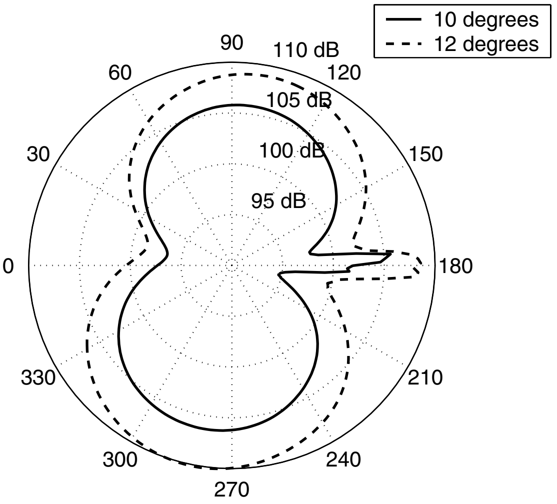

Fig. 15 Directivity pattern at a distance of 12 chords from the airfoil center for flow past a NACA 0015 airfoil with a chord of 10 cm at a Reynolds number of 1.6 × 10^5, a Mach number of 0.2, and angles of attack of 10 and 12 deg.

level between a NACA 0012 airfoil and a NACA 0024 airfoil at $M = 0.3$ and an angle of attack of 4 deg is almost negligible (less than 1 dB), but the difference increases substantially when the Mach number increases to $M = 0.8$. To analyze the difference in sound pressure level between a NACA 0012 airfoil and a NACA 0015 airfoil, computations at $M = 0.2$ are carried out for flow past a NACA 0012 airfoil at $Re = 5 \times 10^5$ and an angle of attack of 16 deg and for flow past a NACA 0015 airfoil at $Re = 1.6 \times 10^5$ and the same angle of attack. The reasons for choosing this angle of attack are as follows:

1) It would take a long time (two months) to perform new computations.

2) Computations for flows at an angle of attack of 16 deg have already been performed.

The corresponding noise spectra are plotted in Fig. 11. The figure shows that the noise levels are very close for frequencies larger than 300 Hz, whereas the noise level at frequencies smaller than 300 Hz from a NACA 0015 airfoil at $Re = 1.6 \times 10^5$ is slightly smaller than from a NACA 0012 airfoil at $Re = 5 \times 10^5$. This may be due to the difference in Reynolds number. From the comparison, we can conclude that the difference in thickness between a NACA 0012 and a NACA 0015 will not produce very different noise spectra for flows at moderate angles of attack.

At an angle of attack of 4 deg, the pressure fluctuations measured at a distance of 12 chords away from the airfoil center are plotted in Fig. 12a. From the figure, we observe that the fluctuations are much stronger than those at 8 deg (see also Fig. 8a). This phenomenon is also observed when examining the noise spectra given by Brook et al. [5] for an untripped NACA 0012 airfoil at small angles of attack. From the diagram on appearance of tonal noise [22,27], the tonal noise for a NACA 0012 airfoil at $Re = 1.6 \times 10^5$ appears at angles of attack smaller than 5 deg. The mechanism of such tonal noise was caused by the existence of a separation bubble near the trailing edge at the pressure side. For more details, the reader is referred to [27]. This feature can also be observed from the fluctuations of the lift force at 4 deg in the flow computations. Note that the absolute mean values of the pressure signals at 4 deg shown in Fig. 12a are smaller than those at 8 deg. Performing a FFT on the signal measured at 90 deg, the sound pressure level is plotted in Fig. 12b. From the figure, it is seen that the frequency spectrum is centered at a frequency of about 2 kHz. This center frequency is much higher than the center frequency (about 500 Hz) for the flow at 8 deg.

The directivity pattern at a distance of 12 chords from the airfoil center for the flow at 4 deg is plotted in Fig. 13. From the figure, we observe the existence of a near dipole, much akin to the near dipole at 8 deg (Fig. 10), and a noise level stronger than that at 8 deg. The axis of the near dipole has an angle of about 5.4 deg from the horizontal axis. The noise level reaches its maximum value at about 82.6 deg. To compare with noise patterns in the literature, we select the directivity pattern made by Zhou and Joseph [42] for a NACA 0012 airfoil at $M = 0.3$ and an angle of attack of 4 deg with frozen incident turbulence (Fig. 8 in [42]). Their noise directivity pattern also shows a near dipole structure with an axis at a very small angle to the horizontal plane. The low-noise region in the downstream direction is quite similar, whereas the low-noise region upstream is wider in our case.

At an angle of attack of 6 deg, the pressure fluctuations are measured at 12 chords away from the airfoil center. By performing FFTs on the signals at 90 and 270 deg, the one-third-octave spectra are obtained and plotted in Fig. 14a. To compare with experiments, we use the experimental noise spectrum published in [5] for flow past a NACA 0012 airfoil with sharp trailing edge at a Reynolds number of 5×10^5 and an angle of attack of 6.7 deg, with an observer located at 90 deg and 12 chords away from the airfoil. The figure shows that the noise levels are very similar except for frequencies greater than 2000 Hz, at which the numerical model systematically predicts a higher level. This high noise level is due to the airfoil bluntness noise that is also observed in Fig. 8b (with almost the same level). In Fig. 14b, the acoustic directivity pattern is shown. From the figure, the structure is seen to be similar to the directivity pattern at 8 deg (see also Fig. 10). The axis of the near dipole attains an angle of about 10.2 deg, as can be seen in Figure 14b.

The noise patterns at angles of attack of 10 and 12 deg are compared in Fig. 15. The figure shows that the noise structure in both cases is almost a dipole. The axis of the near dipole at an angle of attack of 10 deg has an angle of about 10 deg from the horizontal plane, whereas the angle increases to 13.4 deg when the angle of attack increases to 12 deg. The maximum noise level and the axis angle β of directivity patterns measured at a distance of 12 chords away from the airfoil center is listed in Table 2 as a function of angle of attack. The table shows that the maximum noise level remains small for angles of attack below 8 deg and increases strongly about 6 dB from 8 to 10 deg.

Conclusions

The splitting technique that consists of dividing the compressible solution into an incompressible flow part and a fluctuating acoustic part is extended to simulate three-dimensional turbulent flows. As acoustic waves are essentially generated by flow unsteadiness, unsteady computations with a suitable subgrid-scale model (the mixed-scale model) are performed for flow past a NACA 0015 airfoil at a Reynolds number of 1.5×10^5 and a Mach number of 0.2. The obtained lift and drag force characteristics are compared with experimental data. The comparisons show good agreements between the computed and measured airfoil lift characteristics for angles of attack below stall, whereas the lift coefficient is slightly overpredicted in the near-stall region. The obtained noise spectra are compared with experimental data and fairly good agreements are seen. The directivity pattern is shown for flows at angles of attack between 4 and 12 deg. From the directivity pattern, it is seen that the noise level is decreasing slightly from 4 to 6 deg, remaining small for angles of attack smaller than 8 deg, increasing sharply with 6 dB from 8 to 10 deg, and reaching a maximal value at 12 deg.

Table 2 Maximum noise levels and axis angle of the near dipole at a distance of 12 chords from the airfoil center for flow past a NACA 0015 airfoil with a chord of 10 cm at a Reynolds number of 1.6 × 10^5 and a Mach number of 0.2

ϕ	4 deg	6 deg	8 deg	10 deg	12 deg
SPL_M	102.8	98.4	99.7	105.8	108.9
β	5.4 deg	10.2 deg	12.2 deg	10 deg	13.4 deg

Acknowledgments

This study was supported partly by the Research Programme for Renewable Energy (EFP-06) and partly by the Danish Scientific Research Council (STVF-04). The computer simulations were performed on a cluster of 210 personal computers, sponsored by the Danish Centre for Scientific Computing.

References

[1] Lighthill, M. J., "On Sound Generated Aerodynamically. 1: General Theory," *Proceedings of the Royal Society of London, Series A: Mathematical and Physical Sciences*, Vol. 211, 1952, pp. 564–587. doi:10.1098/rspa.1952.0060

[2] Curle, N., "The Influence of Solid Boundaries upon Aerodynamic Sound," *Proceedings of the Royal Society of London, Series A: Mathematical and Physical Sciences*, Vol. 231, 1955, pp. 505–514. doi:10.1098/rspa.1955.0191

[3] Ffowcs Williams, J. E., and Hawkings, D. L., "Sound Generation by Turbulence and Surfaces in Arbitrary Motion," *Philosophical Transactions of the Royal Society of London, Series A: Mathematical and Physical Sciences*, Vol. 264, 1969, pp. 321–342. doi:10.1098/rsta.1969.0031

[4] Howe, M. S., "A Review of the Theory of Trailing Edge Noise," *Journal of Sound and Vibration*, Vol. 61, No. 3, 1978, pp. 437–465. doi:10.1016/0022-460X(78)90391-7

[5] Brook, T. F., Pope, D. S., and Marcolini, M. A., "Airfoil Self-Noise and Prediction," NASA Ref. Publ. 1218, 1989.

[6] Lowson, M. V., "Assessment and Prediction of Wind Turbine Noise," Flow Solutions Rept. 92/19, W/13/00284/REP, Bristol, England, U.K., 1992.

[7] Grosveld, F. W., "Prediction of Broadband Noise from Horizontal Axis Wind Turbines," *Journal of Propulsion and Power*, Vol. 1, No. 4, 1985, pp. 292–299. doi:10.2514/3.22796

[8] Viterna, L. A., "The NASA LeRC Wind Turbine Sound Prediction Code," NASA CP-2185, 410, 1981.

[9] Fuglsang, P., and Madsen, H. A., "Implementation and Verification of an Aeroacoustic Noise Prediction Model for Wind Turbines," Risø National Lab., Rept. Risø-R-867 (EN), Roskilde, Denmark, 1996.

[10] Wagner, S., Bareiss, R., and Guidati, G., "Wind Turbine Noise (EUR 16823)," Springer, New York, 1996.

[11] Zhu, W. J., Heilskov, N., Shen, W. Z., and Sørensen, J. N., "Modeling of Aerodynamically Generated Noise from Wind Turbines," *Journal of Solar Energy Engineering*, Vol. 127, No. 4, 2005, pp. 517–528. doi:10.1115/1.2035700

[12] Goody, M., "Empirical Spectral Model of Surface Pressure Fluctuations," *AIAA Journal*, Vol. 42, No. 9, 2004, pp. 1788–1794. doi:10.2514/1.9433

[13] Wagner, C., Hüttl, T., and Sagaut, P., *Large Eddy Simulation for Acoustics*, Cambridge Univ. Press, New York, 2007.

[14] Smith, D. L., Paxson, R. P., Talmadge, R. D., and Hotzo, E. R., "Measurements of the Radiated Noise from Airplanes," US Air Force Flight Dynamics Lab., Rept. TM-70-3-FDAA, Wright–Patterson AFB, OH, 1970.

[15] Clark, L. T., "The Radiation of Sound from an Airfoil Immersered in a Laminar Flow," *Journal of Engineering for Power*, Vol. 93, No. 4, 1971, pp. 366–376.

[16] Hersh, A. S., and Hayden, R. E., "Aerodynamic Sound Radiation from Lifting Surfaces with and Without Leading Edge Serrations," NASA CR-114370, 1971.

[17] Paterson, R. W., Vogt, P. G., and Fink, M. R., "Vortex Noise of Isolated Airfoil," AIAA Paper 72-656, 1972.

[18] Sunyach, M., Arbey, H., Robert, D. Bataille, J., and Comte-Bellot, G., "Correlations Between Far-field Acoustic Pressure and Flow Characteristics for a Single Airfoil," AGARD CP 131, Paper 5, Neuilly-sur-Seine, France, 1973.

[19] Tam, C. K. W., "Discrete Tones of Isolated Airfoil," *Journal of the Acoustical Society of America*, Vol. 55, No. 6, 1974, pp. 1173–1177.

[20] Fink, M. R., "Prediction of Airfoil Tone Frequencies," *Journal of Aircraft*, Vol. 12, No. 2, 1975, pp. 118–120. doi:10.2514/3.44421

[21] Arbey, H., and Bataille, J., "Noise Generated by Airfoil Profiles Placed in a Uniform Laminar Flow," *Journal of Fluid Mechanics*, Vol. 134, No. -1, 1983, pp. 33–47. doi:10.1017/S0022112083003201

[22] Lowson, M. V., Fiddes, S. P., and Nash, E. C., "Laminar Boundary Layer Aeroacoustic Instabilities," AIAA Paper 94-0358, 1994.

[23] Nash, E. C., and Lowson, M. V., "Noise Due to Boundary Layer Instabilities," *CEAS/AIAA Aeroacoustics Conference*, Munich, Paper 95-124, 1995.

[24] Lowson, M. V., McAlpine, A., and Nash, E. C., "The Generation of Boundary Layer Instability Noise on Aerofoils," AIAA Paper 98-0626, 1998.

[25] McAlpine, A., Nash, E. C., and Lowson, M. V., "On the Generation of Discrete Frequency Tones by the Flow Around an Aerofoil," *Journal of Sound and Vibration*, Vol. 222, No. 5, 1999, pp. 753–779. doi:10.1006/jsvi.1998.2085

[26] Nash, E. C., Lowson, M. V., and McAlpine, A., "Boundary-Layer Instability Noise on Aerofoils," *Journal of Fluid Mechanics*, Vol. 382, 1999, pp. 27–61. doi:10.1017/S002211209800367X

[27] Desquesnes, G., Terracol, M., and Sagaut, P., "Numerical Investigation of the Tone Noise Mechanism over Laminar Airfoils," *Journal of Fluid Mechanics*, Vol. 591, 2007, pp. 155–182.

[28] Sandberg, R. D., and Sandham, N. D., "Direct Numerical Simulations of Trailing-Edge Noise Generated by Turbulent Boundary-Layers," AIAA Paper 2007-1037, 2007.

[29] Wang, M., and Moin, P., "Computation of Trailing-Edge Flow and Noise Using Large-Eddy Simulation," *AIAA Journal*, Vol. 38, No. 12, 2000, pp. 2201–2209. doi:10.2514/2.895

[30] Marsden, O., Bogey, C., and Bailly, C., "Direct Noise Computation of the Turbulent Flow Around a Zero-Incidence Airfoil," *AIAA Journal*, Vol. 46, No. 4, 2008, pp. 874–883. doi:10.2514/1.29825

[31] Shen, W. Z., and Sørensen, J. N., "Aero-Acoustic Modeling of Turbulent Airfoil Flows," *AIAA Journal*, Vol. 39, No. 6, 2001, pp. 1057–1064. doi:10.2514/2.1446

[32] Ta Phuoc, L., "Modèles de Sous Maille Appliqués aux Ecoulements Instationnaires Décollés," *Proceedings of the DRET Conference: Aérodynamique Instationnaire Turbulente-Aspects Numériques et Expérimentaux*, Lab. d'Informatique pour la Mécanique et les Sciences de l'Ingénieur, Centre National de la Recherche Scientifique, Rept. 93074, Orsay, France, 1994, pp. 1–38.

[33] Tenaud, C., Pellerin, S., Dulieu, A., and Ta Phuoc, L., "Large Eddy Simulations of a Spatially Developing Incompressible 3-D Mixing Layer Using the v-ω Formulation," *Computers and Fluids*, Vol. 34, No. 1, 2005, pp. 67–96. doi:10.1016/j.compfluid.2004.03.003

[34] Bardina, J., Ferziger, J. H., and Reynolds, W. C., "Improved Subgrid Scale Models for Large Eddy Simulation," AIAA Paper 80-1357, 1980.

[35] Sagaut, P., *Large Eddy Simulation for Incompressible Flows*, 3rd ed., Springer, New York, 2006.

[36] Michelsen, J. A., "Basis3D-a Platform for Development of Multiblock PDE Solvers," TR AFM 92-05, Technical Unv. of Denmark, Lyngby, Denmark, 1992.

[37] Sørensen, N. N., "General Purpose Flow Solver Applied to Flow over Hills," Risø National Lab., Rept. Risø-R-827-(EN), Roskilde, Denmark, 1995.

[38] Shen, W. Z., Michelsen, J. A., and Sørensen, J. N., "An improved Rhie–Chow Interpolation for Unsteady Flow Computations," *AIAA Journal*, Vol. 39, No. 12, 2001, pp. 2406–2409. doi:10.2514/2.1252

[39] Shen, W. Z., Michelsen, J. A., Sørensen, N. N., and Sørensen, J. N., "An Improved SIMPLEC Method on Collocated Grids for Steady and Unsteady Flow Computations," *Numerical Heat Transfer*, Vol. 43, No. 3, Part. B, 2003, pp. 221–239.

[40] Shen, W. Z., Michelsen, J. A., and Sørensen, J. N., "A Collocated Grid Finite Volume Method for Aero-Acoustic Computations of Low-Speed Flows," *Journal of Computational Physics*, Vol. 196, No. 1, 2004, pp. 348–366. doi:10.1016/j.jcp.2003.11.006

[41] Sheldahl, R. E., and Klimas, P. C., "Aerodynamic Characteristics of Seven Airfoil Sections Through 180 Degrees Angle of Attack for Use in Aerodynamic Analysis of Vertical Axis Wind Turbines," Sandia National Labs., Rept. SAND80-2114, Albuquerque, NM, 1981.

[42] Zhou, Q. D., and Joseph, P., "A Frequency Domain Numerical Method for Airfoil Broadband Self-Noise Prediction," *Journal of Sound and Vibration*, Vol. 299, No. 3, 2007, pp. 504–519. doi:10.1016/j.jsv.2006.06.061

D. Gaitonde
Associate Editor